Quantitative Determination of Native Point-Defect Concentrations at the ppm Level in Un-Doped BaSnO₃ Thin Films

*Kendra S. Belthle, Ute N. Gries, Michael P. Mueller, Dennis Kemp, Abhinav Prakash, Marc-André Rose, Jacqueline M. Börgers, Bharat Jalan, Felix Gunkel, and Roger A. De Souza**

The high-mobility, wide-bandgap perovskite oxide BaSnO₃ is taken as a model system to demonstrate that the native point defects present in un-doped, epitaxial thin films grown by hybrid molecular beam epitaxy can be identified and their concentrations at the ppm level determined quantitatively. An elevated-temperature, multi-faceted approach is shown to be necessary: oxygen tracer diffusion experiments with secondary ion mass spectrometry analysis; molecular dynamics simulations of oxygen-vacancy diffusion; electronic conductivity studies as a function of oxygen activity and temperature; and Hall-effect measurements. The results indicate that the oxygen-vacancy concentration cannot be lowered below $10^{17.3}$ cm⁻³ because of a background level of barium vacancies (of this concentration), introduced during film growth. The multi-faceted approach also yields the electron mobility over a wide temperature range, coefficients of oxygen surface exchange and oxygen-vacancy diffusion, and the reduction enthalpy. The consequences of the results for the lowest electron concentration achievable in BaSnO₃ samples, for the ease of oxide reduction and for the stability of reduced films with respect to oxidation, are discussed.

1. Introduction

Since the beginning of the defect age close to a century ago, it has been a challenging task to determine the types and densities of point defects in an oxide.[1–4] By definition, point defects are (rare) deviations from the 3D repetition of the ideal crystal

K. S. Belthle, U. N. Gries, M. P. Mueller, D. Kemp, R. A. De Souza
Institute of Physical Chemistry
RWTH Aachen University
52056 Aachen, Germany
E-mail: desouza@pc.rwth-aachen.de

A. Prakash, B. Jalan
Department of Chemical Engineering and Materials Science
University of Minnesota
Minnesota, MN 55455, USA

M.-A. Rose, J. M. Börgers, F. Gunkel
Peter Gruenberg Institute (PGI 7)
Forschungszentrum Juelich GmbH
52428 Juelich, Germany

structure, and in many oxides, their densities are determined by inadvertently included impurities. The advent of fabrication methods, such as molecular beam epitaxy (MBE), that employ exceptionally pure starting materials and that minimize the possibilities for impurity incorporation have raised the level of the challenge. Negligible concentrations of impurities result in native point defects governing the oxide's defect structure, and the detection of such defects is far from trivial. Furthermore, methods such as MBE produce samples in the form of thin films, and the small volume of material available for analysis constitutes an additional challenge.

One oxide system in which the types and densities of point defects in thin-film samples have attracted attention is the perovskite oxide BaSnO₃. Its high electron conductivity,[5,6] with thin films displaying higher values than even single crystals,[7] makes it a promising candidate for high-power oxide electronics,[8] and the combination of high conductivity[7,9,10] and a bandgap[11–13] of ≈3 eV, which yields optical transparency in the visible range, has established BaSnO₃ as an outstanding transparent conducting oxide (TCO).[14] High electron densities in BaSnO₃ have been achieved by donor doping[5,7] (e.g., doping La onto the Ba site), by reducing the oxide[15,16] (i.e., creating electrons and oxygen vacancies), and by interfacial charge-transfer.[17,18] The lower limit of achievable electron density appears to be (10^{17} to 10^{18}) cm⁻³, below which insulating transport behavior is observed.[7,10,15] These studies have focused, however, on the analysis of electron transport at low temperatures and hence provide only indirect information.

Determining the majority point defects present in an oxide and their densities requires in general not just one method that is sensitive to defects but a variety of methods. Since many defect-sensitive methods are available, the critical question is the optimal choice of methods. In this study, we show that oxygen tracer diffusion experiments, molecular dynamics simulations, electronic conductivity studies, and Hall-effect measurements provide a powerful combination for determining the majority point defects in high-purity oxide thin films. This specific combination of methods is required for several reasons, as will become clear, but the main reason is that the two important, experimentally measured quantities—the oxygen

ADVANCED
SCIENCE NEWS
www.advancedsciencenews.com

ADVANCED
FUNCTIONAL
MATERIALS
www.afm-journal.de

tracer diffusion coefficient, D^*, and the electronic conductivity, σ_n—while sensitive to the presence of point defects, do not yield defect concentrations directly. In both cases, they are the product of a defect concentration (the oxygen-vacancy concentration c_v and the electron concentration n, respectively) and a defect diffusivity or a defect mobility. That is,

$$D^* = f^* D_v c_v / c_O \tag{1}$$

where f^* is the tracer correlation coefficient, D_v is the vacancy diffusivity, and c_O is the concentration of oxygen ions; and

$$\sigma_n = ne\mu_n \tag{2}$$

where e is the electronic charge and μ_n the electron mobility. The molecular-dynamics simulations and the Hall-effect measurements provide D_v and μ_n, respectively.

One major benefit of our study is that it also yields a range of kinetic and thermodynamic data for BaSnO$_3$: the electron mobility μ_n over a wide temperature range, the oxygen-vacancy diffusivity D_v as a function of temperature, and the reduction enthalpy of the oxide ΔH_{red}. In order to discuss these quantities and place them in a wider context, we compare the data obtained for BaSnO$_3$ with the corresponding literature data for SrTiO$_3$, a close member of the perovskite family and one of the few members for which such data are available.

2. Results

2.1. Possible Impurities and Defects

In line with the exceptional purity of MBE-grown films, depth profiles of BaSnO$_3$ thin films by secondary ion mass spectrometry (SIMS) detected no cation impurities. Specifically, secondary ion intensities were at the level of background noise for Al, Mg, and Fe, common acceptor impurities in oxide perovskites. Since the appropriate SIMS standards are not available, we cannot convert these limiting secondary ion intensities into concentrations, and hence, we cannot give upper limits for the amounts of impurities in our samples. We do note, however, that SIMS analyses[19] of un-doped SrTiO$_3$ single crystals revealed Al as an impurity at a level of $\approx 10^{17}$ cm^{-3}. We tentatively suggest, therefore, that if cation impurities were present in our films at a level of $\approx 10^{17}$ cm^{-3}, they would have been detected.

In the absence of significant concentrations of impurities, native defects will determine the defect chemistry, and there are five native disorder reactions.[20–22] Given the close-packed nature of the perovskite structure, Frenkel, anti-Frenkel, and anti-Schottky disorder reactions will have prohibitively high energies, and thus, interstitial defects (Ba$_i$, Sn$_i$, O$_i$ in Kröger–Vink notation[21,23]) will not be present in significant amounts. This leaves Schottky disorder reactions and antisite disorder reactions as possible dominant defect reactions, and thus five possible native defects (relative charges are not indicated as various charge states are possible): oxygen vacancies (v$_O$), barium vacancies (v$_{Ba}$), tin vacancies (v$_{Sn}$), barium antisites (Ba$_{Sn}$), and tin antisites (Sn$_{Ba}$). The four cation defects will arise from miniscule imbalances in the Ba:Sn ratio during synthesis. As

cation defects in a perovskite oxide, they will only be mobile at very high temperatures ($T > 1200$ K),[24–28] and thus can be considered frozen in at lower temperatures, resulting in a fixed background concentration of native cation defects. If ionized, the first three cation defects (v$_{Ba}$, v$_{Sn}$, Ba$_{Sn}$) are acceptor-type defects, the fourth (Sn$_{Ba}$) is a donor-type defect.

2.2. Electrical Studies

The quantity sought through these studies is the equilibrium electron concentration in the films, n, as a function of temperature T and oxygen activity aO_2. Hall-effect measurements would generally be the method of choice, but our Hall-effect apparatus is limited at elevated temperatures to Ar atmospheres ($aO_2 \approx 10^{-5}$). The conditions of interest for un-doped BaSnO$_3$, however, are high temperatures and more reducing conditions ($10^{-18} \leq aO_2 \leq 10^{-8}$), meaning that $n(T, aO_2)$ for un-doped BaSnO$_3$ is not directly accessible. We took, therefore, an indirect, two-step route: measuring the conductivity of un-doped samples under the desired low oxygen activities and determining the mobility of a purposely doped sample under the accessible moderately oxidizing conditions of the Hall setup.

The equilibrium conductivity of an un-doped BaSnO$_3$ thin film is shown as a function of oxygen activity in **Figure 1**. Describing the isothermal data with a power-law, $\sigma \propto (aO_2)^m$, we find that the exponent is close to $m = -1/4$ at lower temperatures and higher oxygen activities, becoming closer to $m = -1/6$ at the highest temperature and lowest oxygen activity. Such behavior is characteristic of an acceptor-doped oxide showing n-type conductivity upon reduction,[29–31] the concentration of electrons (and doubly charged oxygen vacancies[32]) increasing with increasing temperature and decreasing oxygen activity. Consequently, charged tin antisites can be excluded as the majority defects, being donor-type defects. As will be demonstrated in Section 3.1, the observation of a transition from $m = -1/4$ to $m = -1/6$ allows the concentration of the (native) acceptor defect to be determined.
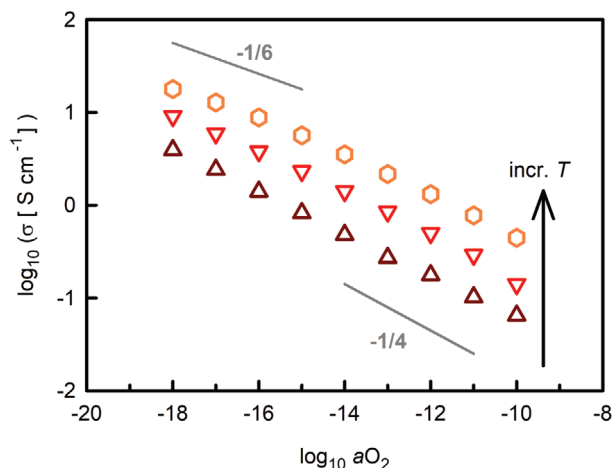

Figure 1. Conductivity σ of a 200-nm thick film of un-doped BaSnO$_3$ as a function of oxygen activity aO_2 at temperatures T/K = 900, 950, 1000. For $aO_2 > 10^{-10}$, the measured conductivity included a substantial contribution from the SrTiO$_3$ substrate.

**ADVANCED
SCIENCE NEWS**

www.advancedsciencenews.com

**ADVANCED
FUNCTIONAL
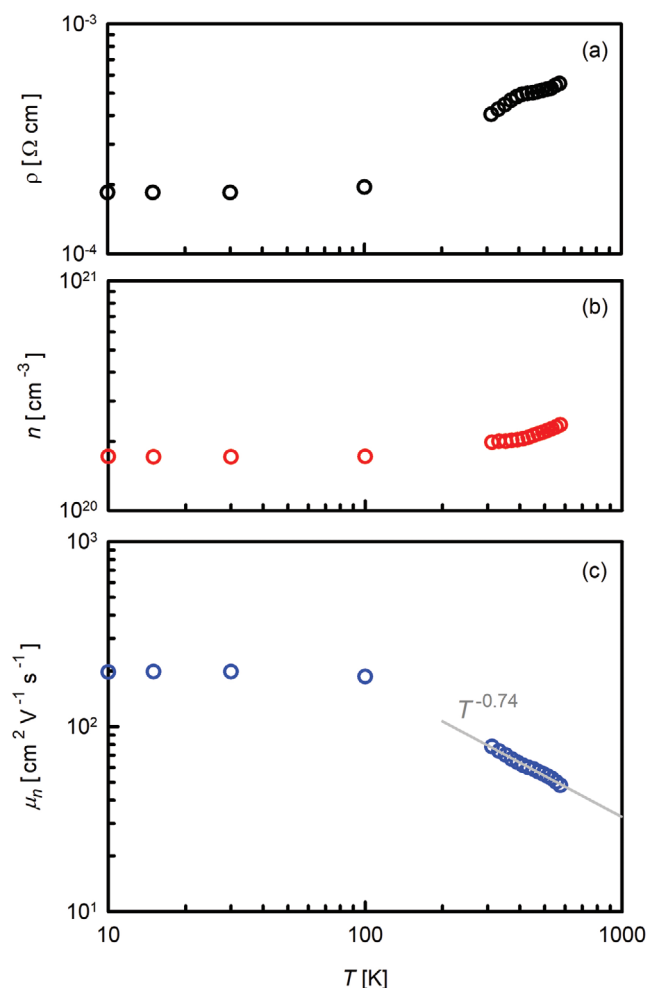MATERIALS**

www.afm-journal.de

Figure 2. Electronic transport in thin-film $BaSnO_3$ doped with 1% La investigated as a function of temperature with low-temperature and high-temperature Hall measurements in the van der Pauw configuration: a) resistivity ρ, b) electron density n, and c) electron mobility μ_n.

The electron mobility was obtained, as noted above, for a doped $BaSnO_3$ thin film (doped with 1 at% La), rather than for un-doped samples, by combining Hall-effect and electrical-resistivity measurements. The high concentration of electrons in such samples allows reliable values to be obtained for μ_n. The results are plotted in **Figure 2** for temperatures $10 \leq T/K \leq 580$. The resistivity is seen to increase slightly with increasing temperature (Figure 2a). From Hall-effect studies (Figure 2b), we observed a constant electron density n at low temperatures and a slight increase above room temperature. The origin of this increase is not clear and is thus left for future studies.

In Figure 2c, we plot μ_n obtained from these data. At low temperatures, the mobility saturates at $\mu_n = 200$ cm^2 $V^{-1}s^{-1}$, a value comparable with the high mobilities reported for $BaSnO_3$ thin films.[7] The saturation of the mobility is consistent with electron scattering from charged defects.[7,33] At elevated temperatures, μ_n decreases with increasing temperature, and it can be described with a power law, μ_n/cm^2 V^{-1} $s^{-1} = 10^{3.731} \times (T/K)^{-0.74}$. Such behavior is characteristic of the mobility being limited by phonon scattering, and it is typically independent of

point-defect densities.[33,34] As a consequence, we can use the power-law expression for the electron mobility in the high-temperature regime to analyze the conductivity data of un-doped $BaSnO_3$, and we do this in Section 3.1.

2.3. Oxygen Diffusion Studies

The primary quantity of interest here is the concentration of oxygen vacancies. Since oxygen diffusion takes place by means of oxygen vacancies in perovskite oxides, studying oxygen diffusion allows us to probe the behavior of oxygen vacancies.

2.3.1. Experimental Determination

In **Figure 3**a, we show a typical isotope diffusion profile obtained for a $BaSnO_3$ thin-film sample. Even at this high temperature ($T = 973$ K) and for this relatively long diffusion time ($t \approx 10$ h), the isotope diffusion front did not penetrate far into the sample, ≈ 50 nm. Visual inspection of the isotope profile suggests that the tracer diffusion coefficient is not spatially invariant, and indeed the best description was found for a position-dependent tracer diffusion coefficient with an increase over the first 10 nm from a low value at the surface to a constant (bulk) value. This behavior is consistent with the presence of a space-charge zone depleted of oxygen vacancies at the surface,[19,35–38] but there are other possible explanations.[39,40] We do not pursue the origin of the lowered diffusivity further here. Numerical solutions to the diffusion equation with spatially varying tracer diffusion coefficients were obtained by finite-element-method (FEM) calculations, as described elsewhere;[19,37] and comparison of the calculated profiles with the measured profiles yielded the surface exchange coefficient k^* and the tracer diffusion coefficient in the bulk, D^*.

Given that epitaxial films of $BaSnO_3$ on $SrTiO_3$ substrates have high densities of dislocations to accommodate the lattice mismatch,[41] it is worth noting that the isotope profiles provide no evidence of faster diffusion of oxygen along dislocations in these films, that is, in no profile was a pronounced third feature at larger depths, the dislocation "tail",[42] observed. In view of experimental and computational work on dislocations in acceptor-doped $SrTiO_3$,[43–46] however, faster diffusion of oxygen along dislocations is not expected in acceptor-doped $BaSnO_3$ (see also Section 3.2).

Values of these two transport parameters obtained as a function of temperature are plotted in Figure 3b,c; two data points were obtained for each exchange temperature, corresponding to two time-of-flight secondary ion mass spectrometry (ToF-SIMS) profiles of the same sample. The activation enthalpy for surface exchange, $\Delta H_{k^*} = (3.1 \pm 0.7)$ eV, is very similar to that obtained for other acceptor-doped, wide bandgap perovskites, such as $SrTiO_3$[19] and $BaTiO_3$;[38,47] the absolute magnitude also appears to be comparable (see Figure S1, Supporting Information). The activation enthalpy obtained for oxygen tracer diffusion, $\Delta H_{D^*} = (1.31 \pm 0.34)$ eV, is substantially higher than values obtained for related cubic $A^{II}B^{IV}O_3$ perovskites, such as $SrTiO_3$[19] and $BaTiO_3$,[38] that are 0.6 to 0.7 eV. The value is comparable, though, with data reported[48] for
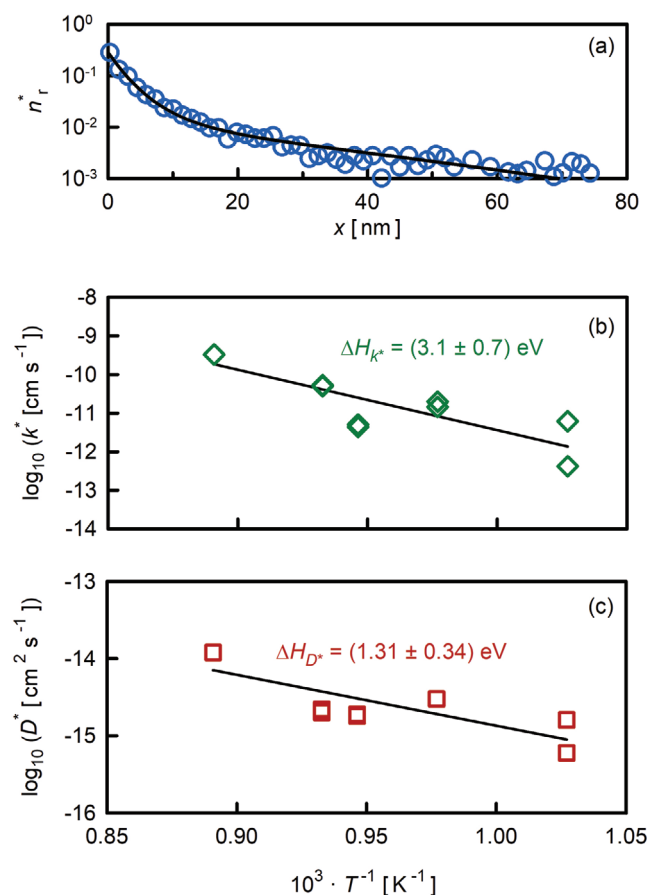
Figure 3. Oxygen tracer diffusion in un-doped BaSnO$_3$ thin films studied by ^{18}O/^{16}O exchange and ToF-SIMS depth profiling under oxidizing conditions (aO$_2$ = 0.2). a) Normalized isotope fraction n_r^* versus depth x obtained after an isotope anneal at T = 973 K for t = 3.66 × 10^4 s. b) Oxygen surface exchange coefficients k^* as a function of inverse temperature. c) Oxygen tracer diffusion coefficients D^* as a function of inverse temperature. In (b) and (c), two data points are plotted at each temperature; they refer to data from two ToF-SIMS profiles on each exchanged sample.

oxygen-ion conduction in BaSnO$_3$-based materials, the activation enthalpy varying from 1.32 to 0.96 eV for BaSn$_{1-y}$Y$_y$O$_{3-y/2}$ (with y = 0.05 − 0.375). The comparison is not straightforward because the thin films refer to a weakly doped system, whereas the literature refers to heavily substituted compounds.

2.3.2. Computational Investigations

From Equation (1), one recognizes that either $D_v(T)$ or $c_v(T)$ is required to interpret experimental $D^*(T)$ data. Molecular-dynamics simulations constitute an optimal method [44,49–51] for obtaining $D_v(T)$. Indeed, classical molecular-dynamics simulations that employ the empirical pair-potentials of Pedone et al.[52] have been shown[44,49] to reproduce experimental diffusion rates of oxygen vacancies in SrTiO$_3$ [19,27,53–55] and BaTiO$_3$[38,56,57] extraordinarily well, not only in terms of the activation enthalpy of oxygen-vacancy migration but also the absolute rate of vacancy diffusion. Here, we used molecular-dynamics simulations with the empirical pair-potentials of Pedone et al.[52] to
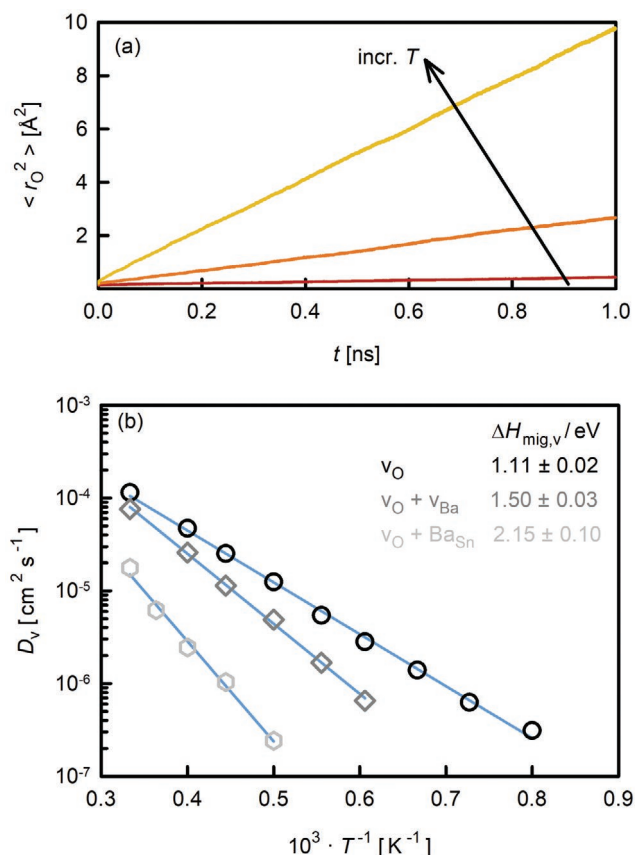

Figure 4. Molecular-dynamics simulations of oxygen tracer diffusion in BaSnO$_3$. a) Mean squared displacement of the oxygen ions, $\langle r_O^2 \rangle$, as a function of time t for three temperatures (T/K = 1500, 2000, 2500) for a cell containing only oxygen vacancies. b) Oxygen-vacancy diffusivity D_v obtained as a function of inverse temperature. Simulation cells contained either v$_O$, v$_O$ and v$_{Ba}$, or v$_O$ and Ba$_{Sn}$, with c_v/c_O = 0.49% in all cases.

calculate $D_v(T)$ in BaSnO$_3$ for four different cases: All simulation cells contained a fixed number of oxygen vacancies (40 distributed randomly over 8232 oxygen-ion sites) and either a background charge or the appropriate number (to compensate the oxygen vacancies' charge) of barium vacancies, barium antisites, or tin vacancies.

From the simulations, we obtained the evolution of the mean-squared displacement of the oxygen ions, $\langle r_O^2 \rangle$, as a function of time, and for those cases for which $\langle r_O^2 \rangle$ increased linearly with time in a smooth fashion (see, e.g., **Figure 4**a), we calculated the tracer diffusion coefficient of oxygen by applying Einstein's relation:

$$D_O^* = \frac{1}{6} \frac{d \langle r_O^2 \rangle}{dt} \tag{3}$$

Since for these simulations c_v/c_O = 0.49%, the diffusivity of oxygen vacancies can be extracted with the help of Equation (1) (assuming f^* = 0.69 for all systems[58]). The results are shown in Figure 4b, together with the activation enthalpies of vacancy migration, $\Delta H_{mig, v} = -k_B(d \ln D_v/d\,T^{-1})$.

Relative to the data obtained for the oxygen vacancies alone (this case corresponds to non-interacting defects), the

isothermal vacancy diffusivity is much lower for systems containing discrete acceptor-type cation species; in addition, the activation enthalpy of oxygen-vacancy migration is much higher. Barium antisite defects are seen to produce stronger effects than barium vacancies. No reliable data were obtained for cells with oxygen vacancies and tin vacancies (increases in $\langle r_O^2 \rangle$ with time were barely evident), and this implies that the effect of tin vacancies on oxygen-vacancy behavior is even more unfavorable, that is, even lower D_v and even higher $\Delta H_{mig, v}$. The general behavior can be attributed to acceptor-type defects increasing the local barriers for oxygen-vacancy migration and trapping oxygen vacancies in their vicinity;[59] it is consistent with data for oxygen-vacancy dynamics in related perovskite oxides.[50,51]

3. Discussion

3.1. Quantitative Determination of Vacancy Concentrations

Our primary aim is to determine the concentration and nature of native defects in $BaSnO_3$ thin films. The behavior of the electrical conductivity upon reduction (Figure 1) is consistent with the presence of acceptor-type point defects and doubly charged oxygen vacancies in the films. Through a quantitative description with a defect chemical model, it is possible to extract the effective concentration of acceptor species. We begin by calculating from the conductivity data (Figure 1) and the mobility data (Figure 2c) the electron concentration $n(T, aO_2)$ in the un-doped films. The calculated values, shown in **Figure 5**a, are in the range $10^{16} < n/cm^{-3} < 10^{19}$. Similar electron densities to those at the upper end of this range were reported for $BaSnO_3$ thin films quenched after a high-temperature reduction in vacuum;[15] we were able to access much lower n than those in quenched samples because we probed the high-temperature equilibrium situation (see later).

The defect chemical model comprises a single defect reaction, the reduction of the oxide:

$$O_O^\times \rightleftharpoons v_O^{\cdot\cdot} + 2e' + \tfrac{1}{2}O_2(g) \tag{4}$$

Since the concentration of oxygen ions can be considered constant, the equilibrium constant of this reaction can be written as:

$$K_{red}(T) = c_v n^2 (aO_2)^{1/2} = K_{red}^0 \exp\left(-\frac{\Delta H_{red}}{k_B T}\right) \tag{5}$$

where K_{red}^0 is the pre-exponential factor and ΔH_{red} is the enthalpy of reduction. The concentrations of oxygen vacancies, electrons, and acceptor species are related through a charge balance for the system, that is

$$2c_v = n + c_{Acc} \tag{6}$$

In this formulation c_{Acc} is the effective concentration of acceptor-type defects (nature unknown), if all these defects bore a single negative charge. Defect chemical modeling consists, then, of specifying numerical values for K_{red}^0, ΔH_{red}, and c_{Acc} and solving Equations (5) and (6) simultaneously for given T and aO_2 to yield n.

Through a least-squared fitting of the defect chemical model to the data in Figure 5a, we obtained $c_{Acc} = (5.5 \pm 1.5) \times 10^{17}$ cm^{-3}, $\Delta H_{red} = (3.57 \pm 0.10)$ eV, and $K_{red}^0 = 10^{64.2\pm1.0}$ cm^{-9}. From the study of Ganguly et al.,[15] one can calculate $\Delta H_{red} = 2.94$ eV; given that this value was obtained from quenched samples, the agreement with our reduction enthalpy of $\Delta H_{red} = (3.57 \pm 0.10)$ eV is satisfactory.

With the defect chemical model and with knowledge of c_{Acc} and $K_{red}(T)$, one can predict defect concentrations for conditions other than those examined experimentally. Figure 5b is a plot of defect concentrations calculated for a wide range of aO_2 at $T = 1000$ K. On traversing the plot from left to right, that is, from reducing to oxidizing conditions, one sees that n decreases continually, changing its dependence on aO_2 from $n \propto (aO_2)^{-1/6}$ to $n \propto (aO_2)^{-1/4}$. One also sees that the oxygen-vacancy concentration decreases in the reducing regime according to $c_v \propto (aO_2)^{-1/6}$, but it does not fall below $c_v = (2.75 \pm 0.75) \times 10^{17}$ cm^{-3} because of the presence of background acceptor-type defects. Not shown in Figure 5b is the behavior of the hole concentration p. This is because the p branch was not probed in the conductivity studies (Figure 1), nor is the information required for its prediction available {$N_{VB}(T)$, $N_{CB}(T)$, and $E_g(T)$—the densities of states at the valence-band and conduction-band edges and the bandgap, cf. ref. [60] for $SrTiO_3$}. Of course, in the region in which $n \propto (aO_2)^{-1/4}$, the hole concentration will rise according to $p \propto (aO_2)^{+1/4}$, but it is unclear how high the p branch will

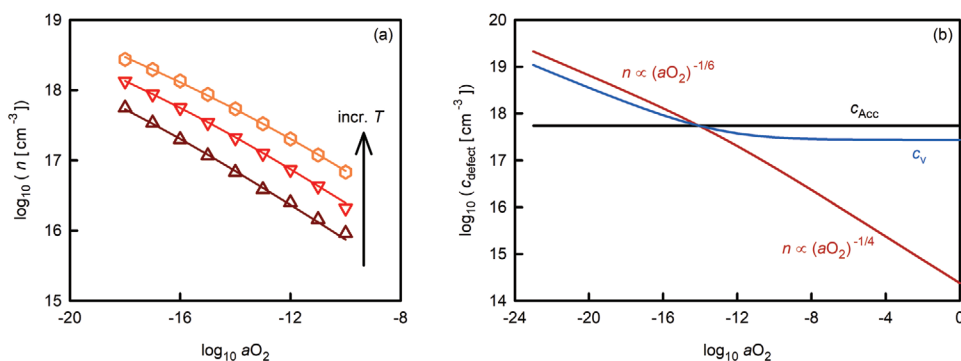**Figure 5.** a) Electron density n as a function of oxygen activity aO_2 at temperatures $T/K = 900, 950, 1000$. Symbols refer to experimental data derived from conductivity and mobility measurements; lines refer to the results of defect chemical modeling. b) Equilibrium defect densities in $BaSnO_3$ as a function of oxygen activity aO_2 at $T = 1000$ K as calculated from defect chemical modeling.

**ADVANCED
SCIENCE NEWS**

www.advancedsciencenews.com

**ADVANCED
FUNCTIONAL
MATERIALS**

www.afm-journal.de

be relative to the n branch. It remains to be seen, therefore, whether dominant p-type conduction is observed at high temperature even in air: The exceptionally high electron mobility may result in dominant n-type conduction even for $n \ll p$.

In order to determine the nature of the acceptor-type cation defects, we make use of the fact that the oxygen-vacancy diffusivity and its activation enthalpy depend on the acceptor-type defects present (Figure 4). Before doing so, we note that the measured activation enthalpy of tracer diffusion can be expressed as the sum of the activation enthalpy of vacancy migration and the generation enthalpy of vacancies, that is, $\Delta H_{D^*} = \Delta H_{mig,v} + \Delta H_{gen,v}$. The generation enthalpy characterizes the dependence of c_v on T, $\Delta H_{gen,v} = -k_B (\mathrm{d} \ln c_v / \mathrm{d} T^{-1})$, and thus can in principle depend on $a\mathrm{O}_2$. In particular, for the oxidizing conditions of the isotope anneals, c_v is constant, fixed by the concentration of acceptor-type point defects, and hence $\Delta H_{gen,v} = 0$. Consequently, for such conditions, $\Delta H_{D^*} = \Delta H_{mig,v}$. (Under reducing conditions, where $2c_v \approx n$, then $\Delta H_{gen,v} = \Delta H_{red}/3$; and $\Delta H_{D^*} = \Delta H_{mig,v} + \Delta H_{red}/3$.)

Since the experimental value of $\Delta H_{D^*} = \Delta H_{mig,v} = (1.31 \pm 0.34)$ eV falls between two cases— non-interacting v_O, $\Delta H_{mig,v} = (1.11 \pm 0.02)$ eV; and v_O and v_{Ba}, $\Delta H_{mig,v} = (1.50 \pm 0.03)$ eV—we consider both cases. With the D_v data of Figure 4b, we only have to specify a value of c_v for each of the two cases so that through Equation (1) the D^* data of Figure 3c can be described. (The molecular-dynamics data have to be extrapolated down to the temperatures of the diffusion experiments, but the small errors obtained for $\Delta H_{mig,v}$ suggest that extrapolation to lower temperatures is acceptable.) **Figure 6** shows that agreement between experiment and simulation can be achieved, requiring in the first case (non-interacting v_O) $c_v = (7.7 \pm 2.0) \times 10^{15}$ cm^{-3} and in the second case (v_O and v_{Ba}) $c_v = (1.3 \pm 0.7) \times 10^{17}$ cm^{-3}. Compared with the vacancy concentration obtained from the conductivity analysis (Figure 5b), the former value is more than one order lower, whereas the latter is rather similar. The comparison of Figure 6 thus indicates that barium vacancies are the native acceptor-type defects present in the films. Taking both approaches (conductivity and diffusion)
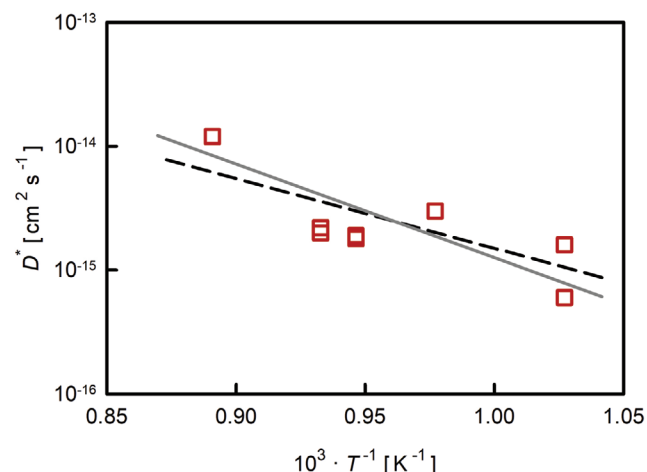
into account, we conclude, therefore, that v''_{Ba} and $v^{\bullet\bullet}_O$ are the dominant point defects in un-doped BaSnO$_3$, confirming the prediction from density-functional-theory (DFT) calculations;[61] and that each defect is present at a concentration of $\approx 2 \times 10^{17}$ cm^{-3}.

Incidentally, the two other cases, Ba$_{Sn}$ and v_{Sn}, can be ruled out for two reasons. The effective activation enthalpies of migration would be too high to explain the experimental data, and since the D_v values are even lower than those for the two other cation defects, the vacancy concentrations would be too high as well.

3.2. Consequences for Point-Defect Behaviour

In view of i) the conclusion that v''_{Ba} and $v^{\bullet\bullet}_O$ are the dominant point defects in un-doped BaSnO$_3$ and ii) the possibility that MBE growth rates are low enough to permit equilibrium to be attained, it is conceivable that the measured vacancy concentrations are equilibrium values. If this is the case, the Gibbs energy of BaO-Schottky disorder in BaSnO$_3$ at the growth temperature can be calculated from $\Delta G_{Sch} = -k_B T \ln[(c_{v_O} c_{v_{Ba}})/(c_O c_{Ba})]$, yielding $\Delta G_{Sch}(T = 1173\,\mathrm{K}) = 2.37$ eV. Although it is not possible to confirm the assumption of equilibrium values from this single set of measurements, the value of ΔG_{Sch} seems physically reasonable, being several eV, and for SrO-Schottky disorder in SrTiO$_3$, $\Delta G_{Sch}(T = 1173\,\mathrm{K}) = 2.61$ eV can be calculated from the data of Moos and Härdtl.[60] Furthermore, if the growth kinetics would determine the defect concentrations, one would expect much higher vacancy concentrations on both cation sublattices.[28,62,63] The assumption of equilibrium values has consequences for the possibilities of lowering the concentration of BaO-Schottky pairs. If chemical equilibrium has been attained, increasing the Ba/Sn ratio during growth will diminish the concentration of v_{Ba} but increase the concentrations of v_{Sn} and Ba$_{Sn}$. The only way of lowering defect concentrations substantially is to lower the growth temperature.

There are also serious consequences for the lowest achievable n in samples quenched from elevated temperatures (see Figure 5b) to room temperature. The critical issue is that defect ionization/trapping equilibria that are unimportant at elevated temperatures can play a central role at room temperature and below.[60,64,65] In the present case, we assume that the key reaction is an electron being trapped by a doubly charged oxygen vacancy to give a singly charged vacancy:

$$v^{\bullet\bullet}_O + e' \rightleftharpoons v^{\bullet}_O \qquad (7)$$
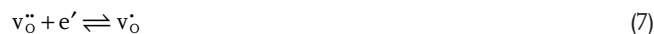
We also assume that, as in SrTiO$_3$,[60] the second trapping reaction, which produces neutral vacancies, has a much smaller trapping enthalpy, and hence can be neglected for most conditions. Our assumption is thus in conflict with a DFT prediction[61] of negative U behavior for $v^{\bullet}_O$, as negative U means[66,67] that singly charged vacancies cannot be the dominant defects at finite temperature. This is, however, only a single prediction, and predictions of negative U behavior in HfO$_2$, for example, vary considerably (see ref. [67] and references therein). What is more important is that, with a physically reasonable assumption, we can achieve a simple, well

Figure 6. Comparison of measured (symbols) and calculated (lines) tracer diffusivities of oxygen in BaSnO$_3$ thin films. The dashed, black line corresponds to non-interacting oxygen vacancies; the solid grey line to oxygen vacancies affected by barium vacancies (see text).

grounded and quantitative explanation of observed behaviour. In order to illustrate the consequences, we differentiate between samples quenched from strongly reducing conditions (e.g., $aO_2 = 10^{-22}$ at $T = 1000$ K in Figure 5b), for which $2c_v \approx n$; and samples quenched from oxidizing conditions (e.g., $aO_2 = 10^{-6}$ at $T = 1000$ K in Figure 5b), for which $c_v \gg n$. For the former case, reaction (7) causes half the available electrons to be trapped upon sample quenching, with essentially all $v_O^{\cdot\cdot}$ becoming $v_O^{\cdot}$. Further trapping cannot take place because the concentration of traps ($v_O^{\cdot\cdot}$) is already exhausted; hence, owing to the concentration ratio $c_v : n$ of 1:2 for the reducing regime, n can only drop to half its initial value upon sample quenching. In contrast, for the latter case, reaction (7) results in the electron concentration dropping by several orders of magnitude because there are far more traps ($v_O^{\cdot\cdot}$) than species to be trapped (e'), the ratio $c_v : n$ in this case being 1:0.027. In this way, we are able to explain why the lowest achievable concentration of electrons at room temperature is (10^{17} to 10^{18}) cm^{-3}. It is because oxygen vacancies are present at this level to compensate barium vacancies, and once $n < c_v$, the doubly charged oxygen vacancies will trap essentially all the electrons upon quenching.

Lastly, since dislocations are often found in thin films of BaSnO$_3$,[41] we mention possible interactions of dislocations with point defects. Here, it is important to make a distinction between acceptor-doped and donor-doped systems, the point-defect structures of the bulk perovskite phases being markedly different.[68,69] The distinction is important because dislocations in perovskite oxides will in general become charged and develop space-charge tubes through their interactions with point defects,[69] and the polarity of the dislocations determines if the mobile charge carriers are depleted or accumulated in the space-charge tubes. Indeed, studies on acceptor-doped SrTiO$_3$ indicate[43–46] positively charged dislocation cores with negatively charged space-charge tubes (depleted $v_O^{\cdot\cdot}$, accumulated e'), arising from the segregation of $v_O^{\cdot\cdot}$ from the bulk to the dislocation cores. For dislocations in donor-doped BaSnO$_3$, v_{Ba}'' appear to segregate to the dislocation cores,[70] which would mean that the dislocations are negatively charged and the space-charge tubes are positively charged (accumulated $v_O^{\cdot\cdot}$, depleted e'). The tracer diffusion results obtained in Section 2.3.1 (no faster diffusion of oxygen observed) are thus consistent space-charge tubes depleted of oxygen vacancies, and thus with positively charged dislocations; consequently, we do not expect to observe any effects of dislocations on σ_n, since the direction of transport is perpendicular, rather than parallel, to the dislocations.[69]

3.3. Characteristic Quantities of Reduced BaSnO$_3$ Relevant for Applications

Having obtained thermodynamic and kinetic data for point defects in BaSnO$_3$, we now discuss the resulting implications for BaSnO$_3$'s use in high-temperature oxide electronics. To this end, we will compare three characteristic quantities (the electron mobility, the reduction enthalpy, and the stability to re-oxidation) with the respective data for the prototypical and closely related perovskite SrTiO$_3$.
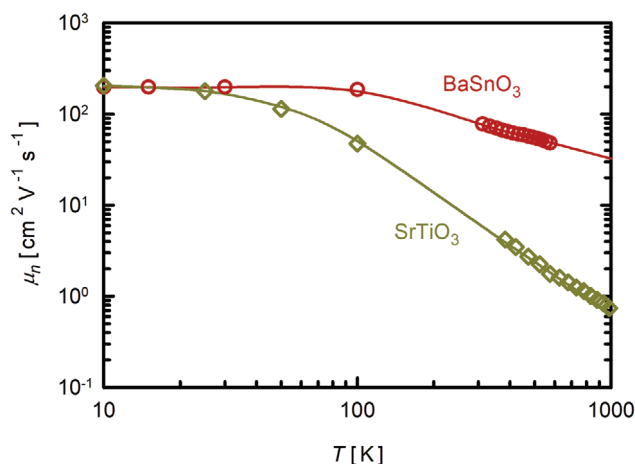

Figure 7. Electron mobility μ_n as a function of temperature T in donor-doped BaSnO$_3$ (1% La$_{Ba}^{\cdot}$, thin film) and donor-doped SrTiO$_3$ (1% Nb$_{Ti}^{\cdot}$, single crystal). Lines are guides to the eye.

3.3.1. Electron Mobility

Figure 7 is a comparison of the electron mobility obtained for donor-doped BaSnO$_3$ and SrTiO$_3$ (with the same nominal donor density of 1%) over a wide range of temperatures. One sees that the μ_n values are comparable in the low-temperature regime but diverge with increasing temperature. At room temperature, BaSnO$_3$ displays a higher electron mobility than SrTiO$_3$ by approximately one order of magnitude; at $T = 500$ K, the difference increases to a factor of 20, and this is predicted by extrapolation to higher temperatures to become a factor of 50 by $T = 1000$ K. For detailed discussions of μ_n in terms of effective masses and phonon scattering, the reader is referred elsewhere.[7,33,34]

3.3.2. Ease of Reduction

The reduction enthalpy of an oxide, referring to the enthalpy of reaction (4), describes the enthalpic cost of creating an oxygen vacancy and two electrons (and half an O$_2$ molecule). It is a material-specific quantity; it does not directly quantify how n varies with temperature. For the reducing regime ($2c_v \approx n$), $\Delta H_{gen,e} = \Delta H_{red}/3$; for the oxidizing regime ($2c_v \approx c_{Acc}$), $\Delta H_{gen,e} = \Delta H_{red}/2$.

In Section 3.1, we obtained $\Delta H_{red} = (3.57 \pm 0.10)$ eV for BaSnO$_3$. In comparison, the reduction enthalpy of SrTiO$_3$ is much higher,[60,71,72] $\Delta H_{red} \approx 6$ eV. In order to emphasize this difference, we calculated from the respective $K_{red}(T)$ the equilibrium oxygen activity required at each temperature to achieve an electron concentration of $n = 10^{19}$ cm^{-3} (assuming $c_{Acc} = 10^{17}$ cm^{-3}). The results are shown in **Figure 8**. At $T = 973$ K, for example, BaSnO$_3$ in equilibrium with $aO_2 \approx 10^{-22}$ exhibits the same n as SrTiO$_3$ in equilibrium with $aO_2 \approx 10^{-34}$. That is, far more extreme conditions are required to achieve the same electron concentration.

Incidentally, while both oxygen activities are very small, the former can be achieved at $T = 973$ K through a mixture of H$_2$
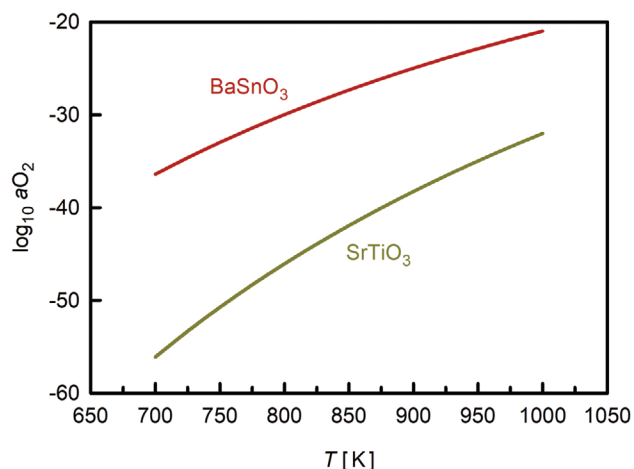
Figure 8. Oxygen activity aO_2 required to achieve at temperature T an electron concentration of $n = 10^{19}$ cm^{-3} calculated from $K_{red}(T)$ for BaSnO$_3$ (this study) and SrTiO$_3$ (ref. [71]).

Figure 9. Equilibration time t_{eq} for a 50-nm thick sample of highly reduced BaSnO$_3$ or SrTiO$_3$ if chemical diffusion of oxygen determines oxidation process. (The RHS axis indicates selected equilibration times in seconds, hours, days and years.)

and H$_2$O at a ratio of $aH_2/aH_2O = 4.16$; if the latter oxygen activity should be achieved through a H$_2$/H$_2$O mixture, the ratio is far more challenging to achieve: It needs to be fixed at $aH_2/aH_2O = 10^{6.4}$.

3.3.3. Equilibration of Reduced Samples

The point-defect structure of acceptor-doped perovskites is substantially different to that of the donor-doped variants.[24,68] As a consequence, the equilibration kinetics of the two types of samples, upon changes in thermodynamic conditions (T, aO_2), are substantially different. Given the focus of this study, we consider the equilibration of reduced acceptor-doped samples. The considerations do not apply, it is stressed, to donor-doped material.

Specifically, we consider the illustrative case of a reduced thin film of BaSnO$_3$ (of thickness $d = 50$ nm) in contact with, say, a more oxidized substrate. The range of temperatures is restricted to $T < 500$ K, so that the rate of oxygen incorporation across the surface is negligible,[55] that is, the sample is shut off from the gas phase. Accordingly, the only source of oxygen is the (more oxidized) substrate, and chemical diffusion of oxygen from the substrate to the film will govern the equilibration. In this case, the time for $\approx 99\%$ change to occur is $t_{eq} = d^2/6D_v$. In the case of a highly reduced film, there are far more oxygen vacancies than barium vacancies (Figure 5b), so that the few barium vacancies present will hardly affect the diffusion of the oxygen vacancies. Thus, it is the diffusivity of isolated oxygen vacancies (see Figure S2, Supporting Information) that is needed to calculate t_{eq}. The results, shown in **Figure 9**, reveal a further advantage of BaSnO$_3$ over SrTiO$_3$: at $T = 340$ K; for example, the conductivity of a reduced SrTiO$_3$ thin film will drop by one order of magnitude in 1 s; the BaSnO$_3$ thin film needs 180 days. That is, because oxygen vacancies are less mobile in BaSnO$_3$, reduced films of this material will maintain a high conductivity for much longer times.
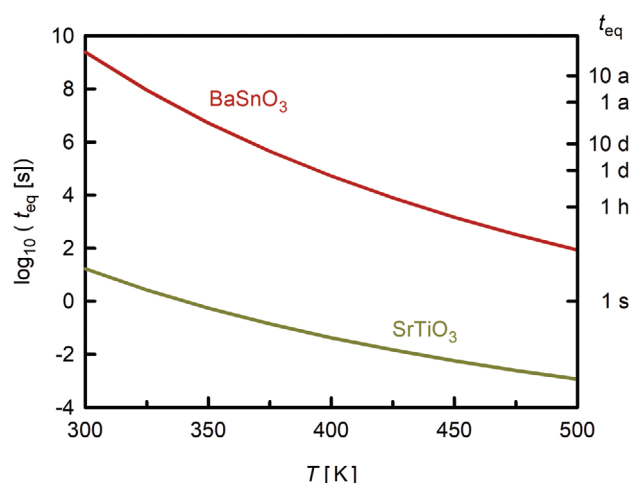
4. Conclusions

There are essentially two levels to this study. The first level is the determination of kinetic and thermodynamic data for point defects in the perovskite oxide BaSnO$_3$ (see **Table 1**). These data indicate quantitatively that BaSnO$_3$ is an excellent material for oxide electronics, not only at room temperature but also at elevated temperatures: It maintains high electron mobility up to high temperatures; it is comparatively easy to reduce, creating high concentrations of electrons; and it is comparatively resistant to re-oxidation, up to moderate temperatures, because oxygen-vacancy migration is rather sluggish. The higher level of this study is the demonstration of how to determine the density and type of native defects in an exceptionally pure thin-film system through a self-contained set of measurements and simulations. The combination of conductivity investigations and Hall-effect measurements allowed us to extract the concentration of acceptor species, and the combination of oxygen tracer diffusion studies and molecular-dynamics simulations allowed us to identify the nature of the acceptor defects. This combination is applicable to all exceptionally pure, wide-bandgap systems: It could, for example, be applied to hybrid organic–inorganic materials, such as methylammonium lead iodide, CH$_3$NH$_3$PbI$_3$. Isolated studies have been already performed,[73–75] but a complete set of data is not available. In

Table 1. Summary of thermodynamic and kinetic data obtained for point defects in BaSnO$_3$.

Quantity	Value	Comment
ΔH_{red}/eV	3.57 ± 0.10	
K^0_{red}/cm^{-9}	$10^{64.2 \pm 1.0}$	
$\Delta G_{Sch}(T = 1173$ K$)$/eV	2.37	BaO-Schottky; equilibrium assumed
μ_n/cm^2 V^{-1} s^{-1}	$10^{3.731} \cdot (T/K)^{-0.74}$	$T > 200$ K
$\Delta H_{mig,\,v}$/eV	$1.11 ; 1.50$	v_O; v_{Ba} and v_O

particular, iodine tracer diffusion experiments performed on the same samples as electrical studies are missing.

In summary, the superior electrical properties of thin-film oxides grown by MBE are often attributed to exceptionally low densities of point defects. Determining the types and densities of these defects in thin films is difficult, however, because of the low densities and because of the small sample volumes. In this study, we determined that vacant sites in a crystal, present at the ppm level, govern its point-defect structure.

5. Experimental Section

MBE Growth: Thin films of un-doped $BaSnO_3$ of thickness $d = 200$ nm were grown on (001)-oriented un-doped $SrTiO_3$ substrates by means of hybrid molecular beam epitaxy, as described elsewhere.[41] As-grown films were electrically insulating at room temperature. Films of La-doped $BaSnO_3$ with the structure La-doped $BaSnO_3$ (40 nm)|$BaSnO_3$ (40 nm)|$SrTiO_3$ were grown for Hall-effect measurements. The temperature of the La cell was 1180 °C.

$SrTiO_3$ was chosen as a substrate for several reasons. First, oxygen diffusion in this substrate is well characterized and understood,[19] thus allowing reliable diffusion coefficients to be extracted, even if the isotope profiles extend into the substrate. Second, oxygen diffusion, even in un-doped material, is relatively fast: Alternative substrates (e.g., MgO) would block oxygen diffusion, if the isotope profiles were long enough to reach the substrate, and this blocking would yield flat isotope profiles within the films, and consequently, unreliable diffusion coefficients. Third, $SrTiO_3$ substrates show low surface roughness over the areas relevant for SIMS analysis (see below). This allows diffusion data to be obtained in high-depth-resolution ToF-SIMS profiles, without surface roughness unduly affecting the diffusion profiles. Finally, although the lattice mismatch between $BaSnO_3$ and $SrTiO_3$ is larger than between, for example, $BaSnO_3$ and MgO, the lattice symmetry does not change (both are cubic perovskites), and this is favourable for film growth.

Conductivity: The high-temperature equilibrium conductivity was measured in four-point geometry in an in-house system, consisting of a tube furnace and a closed yttria-stabilized zirconia oxygen pump to control the oxygen activity. At temperatures of $900 \leq T/K \leq 1000$, the oxygen activity was varied in the range $1 \geq aO_2 \geq 10^{-18}$ with a feedback control of the Nernst voltage dropping between probing volume and reference gas (air). After a change in aO_2 or T, the conductance response of the sample was monitored; the equilibrium conductance was the value obtained when no further change was observed (typically 1–2 h at given aO_2 and T). Since these measurements yield the total conductance of the sample, there is the possibility of a contribution from the (nominally insulating) substrate. In order to obtain the film's conductivity, the substrate's conductance was measured separately and this contribution subtracted from the total conductance. Evaluation of the data indicated that the conductivity of $BaSnO_3$ could be reliably obtained for $-20 \leq \log aO_2 \leq -10$, for which the bare substrate's conductance was significantly lower than that of the $BaSnO_3$|$SrTiO_3$ samples.

Hall Measurements: The van der Pauw configuration was employed for all Hall measurements. Sputtered Pt pads were used as contacts to the sample and bonded by Al wires to the Hall setup. A Lakeshore 8000 high-temperature Hall setup was operated in AC mode, with a magnetic field of 1.2 T and a frequency of 100 mHz. The Hall voltage was measured with a lock-in technique, thereby decreasing noise during elevated temperature measurements. The sample was heated in an Ar atmosphere ($aO_2 \approx 10^{-5}$) in order to prevent corrosion of the setup. Low-temperature Hall measurements were carried out in a standard Quantum Design 9T-PPMS; a linear field-dependence of the Hall voltage between ±9 T was confirmed.

Tracer Diffusion and SIMS: The standard procedure for introducing an oxygen isotope profile into a solid was used.[76–79] Prior to an isotope exchange, a sample was annealed at the temperature T and oxygen activity aO_2 of interest in oxygen of natural isotopic abundance for a duration of 10 times the exchange time. It was then quenched to room temperature. For the isotope anneal, the sample was annealed, at the same temperature T and oxygen activity aO_2, for the exchange time t in ^{18}O-enriched oxygen gas. The sample temperature was monitored by a Pt–Pt/Rh thermocouple situated directly under the sample.

All diffusion profiles were measured by ToF-SIMS[35] on a TOFSIMS IV machine (IONTOF GmbH, Münster, Germany). 25 keV Ga^+ ions, rastered over $100\,\mu m \times 100\,\mu m$, were used to generate secondary ions for ToF analysis, and 2 keV Cs^+ ions, rastered over $300\,\mu m \times 300\,\mu m$, were used for sputter etching of the sample; a beam of electrons with ≈ 20 eV was used for charge compensation. Negative secondary ions were detected with a cycle time of 40 µs.

Solutions of the diffusion equation are formulated in terms of the corrected isotope fraction $n_r^* = (n^* - n_{bg}^*)/(n_g^* - n_{bg}^*)$, where n^* is the isotope fraction determined by TOF-SIMS analysis, n_g^* is the isotope fraction in the annealing gas, and n_{bg}^* is the isotope fraction in a sample that has been equilibrated but not exchanged.[77] Crater depths were determined post-analysis by interference microscopy on a Wyco NT1100 (Veeco Instruments Inc., Plainview, NY, USA).

Molecular-Dynamics Simulations: In order to obtain reliable diffusion data at reasonable temperatures, a large simulation cell was employed, which consisted of $14 \times 14 \times 14$ unit cells of cubic $BaSnO_3$ ($Ba_{2744}Sn_{2744}O_{8232}$), and long simulation runs of 1 ns.[49] The large cell also allowed more than a single point defect to be introduced, while still keeping the defect concentrations within the dilute limit.[49] Molecular-dynamics simulations were performed within the NpT ensemble, that is, particle number N, pressure p, and temperature T were held constant, while energy U and volume V were allowed to vary. The system's temperature (pressure) was controlled by means of a Nose–Hoover thermostat (barostat), with damping parameters of 1 ps (20 ps). A timestep of 1 fs was used. The largescale atomic/molecular massively parallel simulator code was used.[80] Point defects were introduced by either removing or replacing ions at random from the simulation cell, which was equilibrated for 50 ps before the production run.

Supporting Information

Supporting Information is available from the Wiley Online Library or from the author.

Conflict of Interest

The authors declare no conflict of interest.

Author Contributions

R.A.D.S. and B.J. initiated the project. Sample preparation was carried out by A.P. and B.J. Diffusion experiments and simulations were

performed and analyzed by K.S.B., U.N.G., M.P.M., D.K., and R.A.D.S. Low-temperature electrical measurements were carried out and analyzed by M.-A.R., J.M.B., and F.G. High-temperature electrical studies and modeling of equilibrium defect concentrations were performed by F.G. The paper was written by R.A.D.S. with contributions from F.G. and B.J., and support from all co-authors. All authors approved the final version of the manuscript.

[1] P. Kofstad, *Nonstoichiometry, Diffusion, and Electrical Conductivity in Binary Metal Oxides*, Wiley-Interscience, Hoboken, NJ **1972**.

[2] D. M. Smyth, *The Defect Chemistry of Metal Oxides*, Oxford University Press, Oxford **2000**.

[3] H. Schmalzried, A. D. Pelton, *Ann. Rev. Mater. Sci.* **1972**, *2*, 143.

[4] F. Gunkel, D. V. Christensen, Y. Z. Chen, N. Pryds, *Appl. Phys. Lett.* **2020**, *116*, 120505.

[5] H. J. Kim, U. Kim, H. M. Kim, T. H. Kim, H. S. Mun, B.-G. Jeon, K. T. Hong, W.-J. Lee, C. Ju, K. H. Kim, K. Char, *Appl. Phys. Express* **2012**, *5*, 061102.

[6] K. Krishnaswamy, B. Himmetoglu, Y. Kang, A. Janotti, C. G. Van de Walle, *Phys. Rev. B* **2017**, *95*, 205202.

[7] A. Prakash, P. Xu, A. Faghaninia, S. Shukla, J. W. Ager, C. S. Lo, B. Jalan, *Nat. Commun.* **2017**, *8*, 15167.

[8] J. Park, H. Paik, K. Nomoto, K. Lee, B.-E. Park, B. Grisafe, L.-C. Wang, S. Salahuddin, S. Datta, Y. Kim, D. Jena, H. G. Xing, D. G. Schlom, *APL Mater.* **2020**, *8*, 011110.

[9] S. Raghavan, T. Schumann, H. Kim, J. Y. Zhang, T. A. Cain, S. Stemmer, *APL Mater.* **2016**, *4*, 016106.

[10] H. Paik, Z. Chen, E. Lochocki, A. Seidner H., A. Verma, N. Tanen, J. Park, M. Uchida, S. Shang, B.-C. Zhou, M. Brützam, R. Uecker, Z.-K. Liu, D. Jena, K. M. Shen, D. A. Muller, D. G. Schlom, *APL Mater.* **2017**, *5*, 116107.

[11] H. Mizoguchi, H. W. Eng, P. M. Woodward, *Inorg. Chem.* **2004**, *43*, 1667.

[12] W. Zhang, J. Tang, J. Ye, *J. Mater. Res.* **2007**, *22*, 1859.

[13] S. A. Chambers, T. C. Kaspar, A. Prakash, G. Haugstad, B. Jalan, *Appl. Phys. Lett.* **2016**, *108*, 152104.

[14] H. He, Z. Yang, Y. Xu, A. T. Smith, G. Yang, L. Sun, *Nano Convergence* **2020**, *7*, 32.

[15] K. Ganguly, A. Prakash, B. Jalan, C. Leighton, *APL Mater.* **2017**, *5*, 056102.

[16] H. M. I. Jaim, S. Lee, X. Zhang, I. Takeuchi, *Appl. Phys. Lett.* **2017**, *111*, 172102.

[17] T. R. Paudel, E. Y. Tsymbal, *Phys. Rev. B* **2017**, *96*, 245423.

[18] A. Prakash, N. F. Quackenbush, H. Yun, J. Held, T. Wang, T. Truttmann, J. M. Ablett, C. Weiland, T.-L. Lee, J. C. Woicik, K. A. Mkhoyan, B. Jalan, *Nano Letters* **2019**, *19*, 8920.

[19] R. A. De Souza, V. Metlenko, D. Park, T. E. Weirich, *Phys. Rev. B* **2012**, *85*, 174109.

[20] W. Schottky, *Z. Phys. Chem.* **1935**, *29B*, 335.

[21] F. Kröger, H. Vink, *Solid State Physics*, vol. 3, Academic Press, Cambridge, MA **1956**, pp. 307–435.

[22] J. Maier, *Angew. Chem. Int. Ed.* **1993**, *32*, 313.

[23] T. Norby, *J. Korean Ceram. Soc.* **2010**, *47*, 19.

[24] R. Meyer, R. Waser, J. Helmbold, G. Borchardt, *Phys. Rev. Lett.* **2003**, *90*, 105901.

[25] K. Gömann, G. Borchardt, M. Schulz, A. Gömann, W. Maus-Friedrichs, B. Lesage, O. Kaïtasov, S. Hoffmann-Eifert, T. Schneller, *Phys. Chem. Chem. Phys.* **2005**, *7*, 2053.

[26] S. Körfer, R. A. De Souza, H.-I. Yoo, M. Martin, *Solid State Sci.* **2008**, *10*, 725.

[27] A. Hackmann, O. Kanert, *Radiat. Eff. Defects Solids* **1991**, *119-121*, 651.

[28] U. N. Gries, M. Kessel, F. V. E. Hensling, R. Dittmann, M. Martin, R. A. De Souza, *Phys. Rev. Mater.* **2020**, *4*, 123404.

[29] N. H. Chan, R. K. Sharma, D. M. Smyth, *J. Electrochem. Soc.* **1981**, *128*, 1762.

[30] N. H. Chan, R. K. Sharma, D. M. Smyth, *J. Am. Ceram. Soc.* **1982**, *65*, 167.

[31] G. M. Choi, H. L. Tuller, *J. Am. Ceram. Soc.* **1988**, *71*, 201.

[32] R. A. De Souza, D. N. Mueller, *Nat. Mater.* **2021**, *20*, 443.

[33] A. Verma, A. P. Kajdos, T. A. Cain, S. Stemmer, D. Jena, *Phys. Rev. Lett.* **2014**, *112*, 216601.

[34] T. K. Truttmann, J.-J. Zhou, I.-T. Lu, A. K. Rajapitamahuni, F. Liu, T. E. Mates, M. Bernardi, B. Jalan, *Commun. Phys.* **2021**, *4*, 241.

[35] R. A. De Souza, J. Zehnpfenning, M. Martin, J. Maier, *Solid State Ionics* **2005**, *176*, 1465.

[36] R.-V. Wang, P. C. McIntyre, *J. Appl. Phys.* **2005**, *97*, 023508.

[37] R. A. De Souza, M. Martin, *Phys. Chem. Chem. Phys.* **2008**, *10*, 2356.

[38] M. Kessel, R. A. De Souza, M. Martin, *Phys. Chem. Chem. Phys.* **2015**, *17*, 12587.

[39] R. A. De Souza, C. Voisin, H. Schraknepper, M. Teusner, M. Kessel, P. Dufour, C. Tenailleau, S. Guillemet-Fritsch, *Phys. Chem. Chem. Phys.* **2014**, *16*, 2568.

[40] M. P. Mueller, R. A. De Souza, *Appl. Phys. Lett.* **2018**, *112*, 051908.

[41] A. Prakash, J. Dewey, H. Yun, J. S. Jeong, K. A. Mkhoyan, B. Jalan, *J. Vac. Sci. Tech. A* **2015**, *33*, 060608.

[42] A. D. Le Claire, A. Rabinovitch, *J. Phys. C: Solid State Phys.* **1981**, *14*, 3863.

[43] V. Metlenko, A. H. H. Ramadan, F. Gunkel, H. Du, H. Schraknepper, S. Hoffmann-Eifert, R. Dittmann, R. Waser, R. A. De Souza, *Nanoscale* **2014**, *6*, 12864.

[44] S. P. Waldow, R. A. De Souza, *ACS Appl. Mater. Interfaces* **2016**, *8*, 12246.

[45] K. K. Adepalli, J. Yang, J. Maier, H. L. Tuller, B. Yildiz, *Adv. Funct. Mater.* **2017**, *27*, 1700243.

[46] H. Schraknepper, T. E. Weirich, R. A. De Souza, *Phys. Chem. Chem. Phys.* **2018**, *20*, 15455.

[47] C. Schwab, H. Schraknepper, R. A. De Souza, *Phys. Rev. Materials* **2021**, *5*, 105001.

[48] Y. Wang, A. Chesnaud, E. Bevillon, G. Dezanneau, *Solid State Ionics* **2012**, *214*, 45.

[49] J. Kaub, J. Kler, S. C. Parker, R. A. De Souza, *Phys. Chem. Chem. Phys.* **2020**, *22*, 5413.

[50] J. M. Börgers, R. A. De Souza, *Phys. Chem. Chem. Phys.* **2020**, *22*, 14329.

[51] E. Robens, R. Rauschen, J. Kaub, J. P. Parras, D. Kemp, C. L. Freeman, R. A. De Souza, *J. Mater. Chem. A* **2022**, *10*, 2388.

[52] A. Pedone, G. Malavasi, M. C. Menziani, A. N. Cormack, U. Segre, *J. Phys. Chem. B* **2006**, *110*, 11780.

[53] D. B. Schwarz, H. U. Anderson, *J. Electrochem. Soc.* **1975**, *122*, 707.

[54] F. Cordero, *Phys. Rev. B* **2007**, *76*, 172106.

[55] R. A. De Souza, *Adv. Funct. Mater.* **2015**, *25*, 6326.

**ADVANCED
SCIENCE NEWS**

www.advancedsciencenews.com

**ADVANCED
FUNCTIONAL
MATERIALS**

www.afm-journal.de

[56] O. Kanert, H. Schulz, J. Albers, *Solid State Commun.* **1994**, *91*, 465.

[57] F. Cordero, F. Trequattrini, D. Quiroga, P. Silva, *J. Alloys Cpds* **2021**, *874*, 159753.

[58] T. Ishigaki, S. Yamauchi, K. Kishio, J. Mizusaki, K. Fueki, *J. Solid State Chem.* **1988**, *73*, 179.

[59] M. Schie, R. Waser, R. A. De Souza, *J. Phys. Chem. C* **2014**, *118*, 15185.

[60] R. Moos, K. H. Härdtl, *J. Am. Ceram. Soc.* **1997**, *80*, 2549.

[61] D. O. Scanlon, *Phys. Rev. B* **2013**, *87*, 161201.

[62] D. J. Keeble, S. Wicklein, R. Dittmann, L. Ravelli, R. A. Mackie, W. Egger, *Phys. Rev. Lett.* **2010**, *105*, 226102.

[63] D. J. Keeble, S. Wicklein, L. Jin, C. L. Jia, W. Egger, R. Dittmann, *Phys. Rev. B* **2013**, *87*, 195409.

[64] R. Waser, *J. Am. Ceram. Soc.* **1991**, *74*, 1934.

[65] H.-I. Yoo, T.-S. Oh, H.-S. Kwon, D.-K. Shin, J.-S. Lee, *Phys. Chem. Chem. Phys.* **2009**, *11*, 3115.

[66] T. Zacherle, A. Schriever, R. A. De Souza, M. Martin, *Phys. Rev. B* **2013**, *87*, 134104.

[67] M. P. Mueller, F. Gunkel, S. Hoffmann-Eifert, R. A. De Souza, *J. Appl. Phys.* **2021**, *129*, 025104.

[68] R. Meyer, A. F. Zurhelle, R. A. De Souza, R. Waser, F. Gunkel, *Phys. Rev. B* **2016**, *94*, 115408.

[69] R. A. De Souza, *Curr. Opin. Solid State Mater. Sci.* **2021**, *25*, 100923.

[70] H. Yun, A. Prakash, T. Birol, B. Jalan, K. A. Mkhoyan, *Nano Lett.* **2021**, *21*, 4357.

[71] R. A. De Souza, F. Gunkel, S. Hoffmann-Eifert, R. Dittmann, *Phys. Rev. B* **2014**, *89*, 241401.

[72] H. Yamada, G. Miller, *J. Solid State Chem.* **1973**, *6*, 169.

[73] A. Senocrate, I. Moudrakovski, G. Y. Kim, T.-Y. Yang, G. Gregori, M. Grätzel, J. Maier, *Angew. Chem. Intl. Ed.* **2017**, *56*, 7755.

[74] D. Barboni, R. A. De Souza, *Energy Environ. Sci.* **2018**, *11*, 3266.

[75] N. Leupold, A. L. Seibel, R. Moos, F. Panzer, *Eur. J. Inorg. Chem.* **2021**, *2021*, 2882.

[76] P. Fielitz, G. Borchardt, *Solid State Ionics* **2001**, *144*, 71.

[77] R. A. De Souza, R. J. Chater, *Solid State Ionics* **2005**, *176*, 1915.

[78] R. A. De Souza, M. Martin, *MRS Bull.* **2009**, *34*, 907.

[79] J. A. Kilner, S. J. Skinner, H. H. Brongersma, *J. Solid State Electrochem.* **2011**, *15*, 861.

[80] S. Plimpton, *J. Comp. Phys.* **1995**, *117*, 1.